







Terahertz-driven magnetization dynamics of bismuth-substituted yttrium iron-gallium garnet thin film near a compensation point

Evgeny A. Mashkovich ^{1,*}, Kirill A. Grishunin,² Anatoly K. Zvezdin,^{3,4,5} Thomas G. H. Blank ²,
Alexander G. Zavyalov ⁶, Paul H. M. van Loosdrecht ¹, Alexandra M. Kalashnikova ⁷ and Alexey V. Kimel ²

¹University of Cologne, Institute of Physics II, Cologne D-50937, Germany

²Radboud University, Institute for Molecules and Materials, Nijmegen 6525 AJ, The Netherlands


³Prokhorov General Physics Institute, Russian Academy of Sciences, Moscow 119991, Russia

⁴P.N. Lebedev Physical Institute of Russian Academy of Sciences, Moscow 119991, Russia

⁵MIREA - Russian Technological University, Moscow 119454, Russia

⁶University of Nizhny Novgorod, Nizhny Novgorod 603022, Russia

⁷Ioffe Institute, St Petersburg 194021, Russia

 (Received 8 August 2022; revised 31 October 2022; accepted 1 November 2022; published 30 November 2022)

Magnetization dynamics of bismuth-substituted yttrium iron-gallium garnet film $(Y_{3-z}Bi_z)[Fe_{2-x}Ga_x][Fe_{3-y}Ga_y]O_{12}$ has been studied using a terahertz pump–optical probe spectroscopy. Two magnetic modes are observed whose frequencies intersect at a magnetization compensation point. The experimental dependence of the excited modes on terahertz pulse polarization, an external magnetic field and the temperature are analyzed. The theoretical description based on symmetry and the Lagrangian formalisms is proposed. Magnetic modes crossing is explained as interplay between exchange and anisotropy energies equally contributing near the compensation point. Simulations based on the Landau-Lifshitz-Gilbert equations show that a difference in magneto-optical susceptibilities of tetrahedral and octahedral iron sublattices can substantially enhance the sensitivity to the magnetic modes.

DOI: [10.1103/PhysRevB.106.184425](https://doi.org/10.1103/PhysRevB.106.184425)

I. INTRODUCTION

Revealing new fundamental principles and mechanisms for the fastest and the least dissipative ways to control electron spins is believed to be the key that unlocks the next revolution in information processing technology resulting, in particular, in an efficient quantum computing [1], spintronics [2], and magnetic data storage [3]. It is natural that for the fastest and the least dissipative spin reorientation, one employs materials with spin resonances having the highest possible frequency. High frequencies of spin resonances reaching several terahertz (THz) even in the zero applied magnetic field are intrinsic for media with antiferromagnetic exchange interaction [4]. On the other hand, recent progress in the development of tabletop high-field pulsed THz sources made it possible to routinely generate short pulses with a peak electric field exceeding 1 MV/cm with a spectrum covering magnetic resonances in many antiferromagnetic materials [5]. Such a single-cycle THz pulse with subpicosecond duration became one of the major contenders for ultimately fast and least-dissipative control of spins in antiferromagnets.

Among media with antiferromagnetic coupling of spins, ferrimagnets stand as particularly promising ones. They combine nonzero net magnetization, thus, having functionality of ferromagnets with high frequencies of magnetic resonances required for bringing spintronics to the THz operation range. A specific feature of some ferrimagnets, a compensation

temperature T_M at which the net magnetization changes its sign [6], opens up an intriguing possibility to control and even switch magnetization [7] by exciting spin dynamics in a vicinity of T_M . Recently, the possibility to excite a magnetic high-frequency eigenmode in a ferrimagnet by a THz pulse has been demonstrated experimentally [8]. However, such excitations in ferrimagnets driven by a strong THz pulse near its compensation point where ferrimagnets closely resemble antiferromagnetic media remains unexplored.

It has been demonstrated that strong electric [9] and magnetic [10] fields of THz pulses can both serve as stimuli for driving spin dynamics. The THz magnetic field can couple resonantly to the eigenmodes of antiferromagnetically ordered spins. A theoretical consideration has identified the magnetic-field derivative torque as the main mechanism to drive magnetization dynamics [11]. This mechanism was experimentally demonstrated in a series of works on different magnets including collinear antiferromagnets [10,12], weak antiferromagnets [12,13], and ferrimagnets [8]. Thus, in this paper we aim at identifying the peculiarity of a THz pulse-ferrimagnetic spin coupling mechanism in a vicinity of the compensation point.

In this article, we experimentally study THz excitation of spins in a ferrimagnetic bismuth-substituted yttrium iron-gallium garnet $(Y_{3-z}Bi_z)[Fe_{2-x}Ga_x][Fe_{3-y}Ga_y]O_{12}$ in the vicinity of the compensation point of the two iron sublattices and demonstrate simultaneous excitation of quasi-ferromagnetic (q-FM) and quasi-antiferromagnetic (q-AFM) modes with comparable amplitudes. We show that the excitation of both modes has a resonant character and is governed by the magnetic-field derivative torque exerted by a THz pulse.

*Corresponding author: mashkovich@ph2.uni-koeln.de

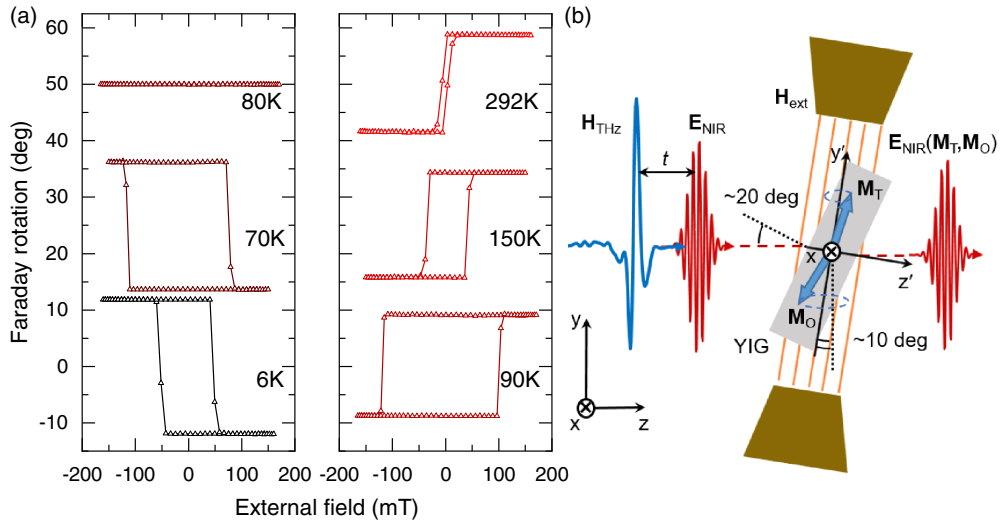


FIG. 1. (a) Magneto-optical hysteresis loops measured at different temperatures. (b) THz pump–NIR probe experimental geometry, top view. The THz and NIR pulses are linearly polarized. The polarization of the THz pump and the NIR probe pulses were controlled by two wire grid polarizers and a half-wave plate, respectively. Two coordinate frames are used: an (xyz) frame linked to the polarization plane (xy) and the propagation direction (z) of the THz pulse, and the $(xy'z')$ frame, where the z' axis is along the NIR probe pulse propagation in the crystal and the y' axis is parallel to the external magnetic-field \mathbf{H}_{ext} .

Comparable effective fields of the exchange interaction and magnetic anisotropy equally contribute to the frequency of spin resonance. A numerical simulation shows that the difference in the magneto-optical susceptibilities of the iron sites enhances the sensitivity of magneto-optical Faraday detection to the magnetic modes.

The paper is organized as follows. Section II reports on the details of the garnet thin film, its characterization, and experimental procedure. Section III describes the main experimental results. Section IV proposes a thermodynamic theory that describes the possible modes of spin resonance in this compound, the temperature dependences of the modes, and the THz-induced torques that can excite them. A simulation based on the numerical solution of the Landau-Lifshitz-Gilbert equations is further used to quantitatively compare the expected magnetization dynamics with experimental observations. The conclusions are summarized in the last section.

II. MATERIALS AND METHODS

The studied sample is a bismuth-substituted yttrium iron-gallium garnet (Bi,Ga-YIG) film grown by liquid phase epitaxy on a gadolinium gallium garnet (GGG) substrate. The substrate orientation is (210), and the film thickness is $10 \mu\text{m}$. The cathodoluminescence characterization shows the content of the film (in at. %): Bi – 6.5, Y – 8.8, Fe – 18.2, Ga – 6.4, and O – 60.1, which corresponds to the composition of $(\text{Y}_{3-z}\text{Bi}_z)[\text{Fe}_{2-x}\text{Ga}_x]^{\text{O}}[\text{Fe}_{3-y}\text{Ga}_y]^{\text{T}}\text{O}_{12}$ with $z = 1.3$ and $x + y = 1.3$ [14] and superscripts denote octahedral (O) and tetrahedral (T) positions. Magnetic moments of iron ions in tetrahedral and octahedral sites form the net magnetizations M_T and M_O , respectively. Replacing a certain amount of iron ions with nonmagnetic gallium ions significantly changes the magnetizations and can lead to emergence of compensation point at temperature T_M at which $M_T(T_M) = M_O(T_M)$ if $1 < x + y < 1.5$ [14]. At the same time, substitution of yttrium

ions with bismuth ions changes the effective spin-orbit coupling and enhances magneto-optical effects [15,16].

To confirm the presence of the compensation point, magneto-optical hysteresis loops at a wavelength of 800 nm were measured at different temperatures. Epitaxial garnet films grown on a (210) GGG substrate possess uniaxial and orthorhombic magnetic anisotropies resulting in the equilibrium orientation of the magnetization tilted away from the sample normal by certain angle which amounts to $\sim 10^\circ$ in the studied film [17]. Therefore, the tilt of the crystal and the orientation of the magnetic field were chosen empirically to maximize the THz-induced probe polarization rotation. Hysteresis loops at several temperatures are shown in Fig. 1(a). The compensation point is clearly observed and estimated to be $T_M \approx 80 \text{ K}$. Using molecular field theory and the value of T_M , one can estimate the gallium substitution on tetrahedral sites y . The values of $y^* \approx 1.152$ and $x^* \approx 0.148$ fit the best (see Appendix A).

In the pump-probe experiment, we use a Ti:sapphire regenerative amplifier with an energy of 4 mJ per pulse, a central wavelength of 800 nm, and a pulse duration of 100 fs at a repetition rate of 1 kHz. The major part of the near infrared (NIR) beam is used to generate THz pump pulses by optical rectification of femtosecond pulses with tilted pulse fronts in lithium niobate [5,18]. A smaller part of the original NIR beam was used as a probe. The NIR probe and THz pump beams are spatially overlapped at the sample surface. The time-resolved THz-induced polarization rotation of the probe beam is measured using a conventional balanced detection scheme and scanning the time-delay t between the THz pump and the NIR probe pulses. To characterize a THz pulse, we use the Pockels effect in a thin [110]-cut GaP crystal [19]. The peak electric field of the THz pulse is estimated to be of 500 kV/cm, which corresponds to the magnetic-field counterpart of $H_{\text{THz}} = 160 \text{ mT}$. The geometry of the experiment is schematically shown in Fig. 1(b).

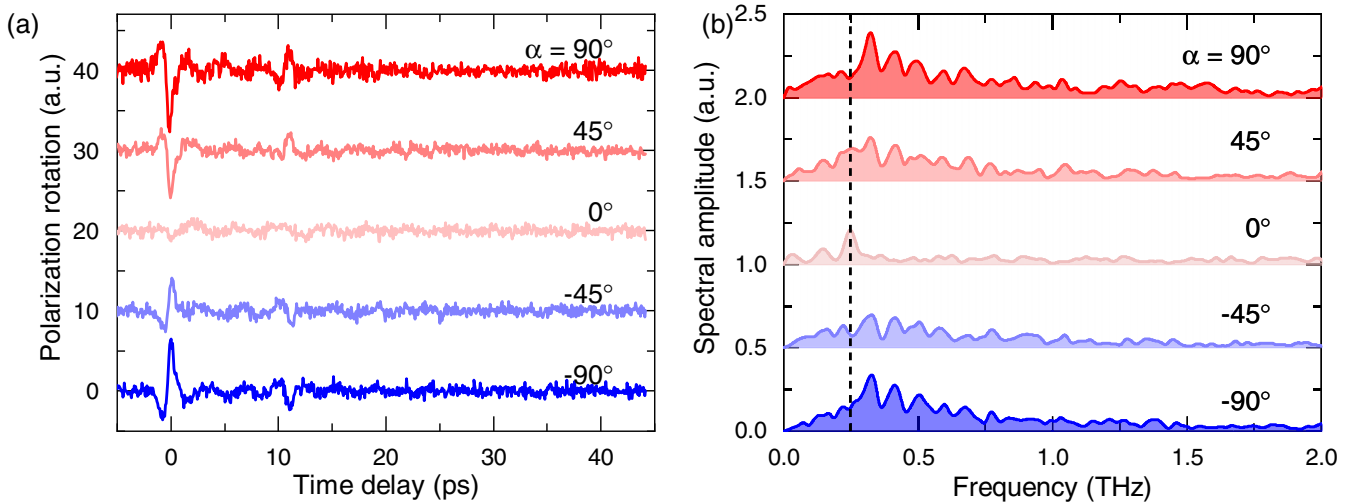


FIG. 2. (a) THz-induced probe polarization rotation for different directions α of the THz magnetic-field \mathbf{H}_{THz} on the xy plane. The orientation angle α is shown next to the corresponding curves. (b) Fourier spectra of the signals from panel (a). The dotted line in (b) marks the spectral position of the narrow-band signal. The shift of the spectrum maximum and narrowing of the bandwidth with α are clearly visible. The measurements were performed at a temperature of $T = 292$ K.

III. RESULTS

Figure 2(a) shows the THz-induced polarization rotation for different directions of a linearly polarized THz magnetic field obtained at room temperature. The direction of the THz magnetic-field $\mathbf{H}_{\text{THz}} = H_{\text{THz}} \sin \alpha \mathbf{x}_0 + H_{\text{THz}} \cos \alpha \mathbf{y}_0$ is controlled on the xy -plane. \mathbf{x}_0 and \mathbf{y}_0 stand for unit vectors along the x and the y axes. At the direction angle of $\alpha = \pm 90^\circ$ ($\mathbf{H}_{\text{THz}} \parallel \mathbf{x}_0$), THz-induced transients show two localized bursts at $t = 0$ and 11 ps resembling the shape of the THz pulse, which can be attributed to a forced THz-induced response. In contrast, at $\alpha = 0^\circ$ ($\mathbf{H}_{\text{THz}} \parallel \mathbf{y}_0$) resolvable oscillation is seen. The fast Fourier transform confirms spectrum narrowing at $\alpha = 0^\circ$ with a peak centered at 250 GHz [Fig. 2(b)], whereas the spectrum at $\alpha = \pm 90^\circ$ is dominated by the broadband signal. The fringes in the spectrum of the broadband signal can be attributed to the backreflection of the THz pulse in the GGG substrate evident from the second burst seen at time delay $t = 11$ ps [see Fig. 2(a)].

To further identify the origin of THz-induced transients, the role of external static magnetic field \mathbf{H}_{ext} was investigated. We set the THz magnetic field $\mathbf{H}_{\text{THz}} \parallel \mathbf{y}_0$ and measured THz-induced rotations at two opposite external magnetic-fields $\pm \mathbf{H}_{\text{ext}}$. Figure 3(a) shows the sum and the difference of the obtained waveforms at these opposing fields. The oscillating narrowband signal dominates the sum waveform and, hence, is even in an external magnetic field [Fig. 3(a)], whereas the small burst attributed to the broadband signal shows an odd dependence. Moreover, the narrow-band signal nearly independent on the absolute value of the external magnetic-field \mathbf{H}_{ext} [Fig. 3(b)]. Interestingly, the broadband signal observed with $\mathbf{H}_{\text{THz}} \parallel \mathbf{x}_0$ is also odd on the reversal of the external magnetic field (see Appendix B). This clearly reveals the difference in the THz-induced transients. Since observation of the oscillating signal at $\alpha = \pm 90^\circ$ ($\mathbf{H}_{\text{THz}} \parallel \mathbf{x}_0$) is obscured by the forced THz-induced response from here on we consider exclusively the geometry with $\mathbf{H}_{\text{THz}} \parallel \mathbf{y}_0$.

Next, we analyze the dependence of the THz-induced polarization rotation on the probe polarization direction. The direction of the electric field of the probe pulse is introduced as $\mathbf{E}_{\text{NIR}} = E_{\text{NIR}} \cos \beta \mathbf{x}_0 + E_{\text{NIR}} \sin \beta \mathbf{y}_0$. The THz-induced transients were strobed by vertically ($\beta = 0^\circ$), horizontally ($\beta = 90^\circ$), and $\beta = 45^\circ$ polarized probe pulses [see Fig. 3(c)]. No pronounced dependence on the probe polarization was revealed, and, thus, we can attribute the THz-induced polarization changes to the Faraday rotation caused by modulation of the antisymmetric part of dielectric permittivity $\varepsilon^{(a)}$. Taking into account low optical absorption of Bi,Ga-YIG at the central wavelength 800 nm of the probe pulse [20] and applying Onsager's principle [21], it can be shown that $\varepsilon^{(a)}$ is an odd function with respect to the magnetization. Limiting our consideration by the term of the lowest order, i.e., assuming that $\varepsilon^{(a)}$ is a linear function of the magnetization, symmetry implies that the THz-induced polarization rotation originates from the oscillations of the out-of-plane component of magnetization along the z' axis. Thus, our experimental observations suggest that THz pump pulses with $\mathbf{H}_{\text{THz}} \parallel \mathbf{y}_0$ excite the magnetic mode characterized by the frequency of 250 GHz at room temperature.

To confirm that the oscillating signal is indeed a fingerprint of the THz-driven magnetic mode, we measured the THz-induced polarization rotation at different temperatures. Figure 4(a) shows the Fourier spectra of the transients obtained at several temperatures as well as their fit using two Lorentzian functions. Figure 4(b) shows the dependence of the central frequencies of the Lorentzian peaks in the spectrum on temperature. Whereas at $T = 292$ K only one peak (red triangles) in the spectrum can be reliably identified in the Fourier spectrum, below $T = 150$ K the second peak emerges (blue circles). One sees that the frequency of the second peak is lower with respect to the frequency of the first peak at $T = 150$ K, has nearly the same value at the compensation point T_M , and is higher at the lower temperature. The peak observed up to room temperature can be attributed to the q-AFM mode (red triangles) of precession of the two sublattices,

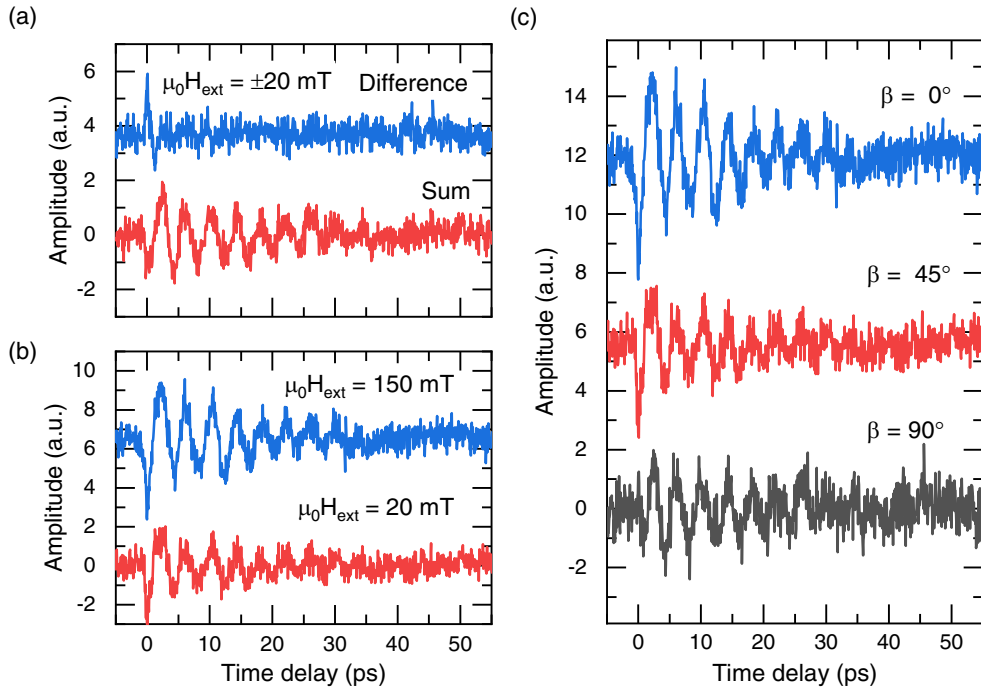


FIG. 3. Sum and difference of the THz-induced polarization rotation measured at opposite polarities of the external magnetic-field $\pm \mathbf{H}_{\text{ext}}$. (b) THz-induced polarization rotations at two external magnetic-field strengths. (c) Dependence on probe polarization angle β , where β is an angle between the probe electrical-field \mathbf{E}_{NIR} and the x axis. $\mathbf{H}_{\text{THz}} \parallel \mathbf{y}_0$ and $T = 292$ K.

whereas the second peak can be attributed to the q-FM mode (blue circles).

IV. THEORETICAL ANALYSIS AND DISCUSSION

Having identified the two magnetic modes excited by the THz pulse, we now turn to a discussion of the possible

excitation mechanism. To characterize the two-sublattice antiferromagnets, we use the Lagrangian approach developed in Ref. [22]. It is conventional to introduce the Néel vector $\mathbf{L} = \mathbf{M}_T - \mathbf{M}_O$ and the net magnetization vector $\mathbf{M} = \mathbf{M}_T + \mathbf{M}_O$ with their absolute values determined as $L = M_O + M_T$ and $M_S = M_O - M_T$, correspondingly. We will use the tilted coordinate system $xy'z'$ depicted in Fig. 1(b). In spherical

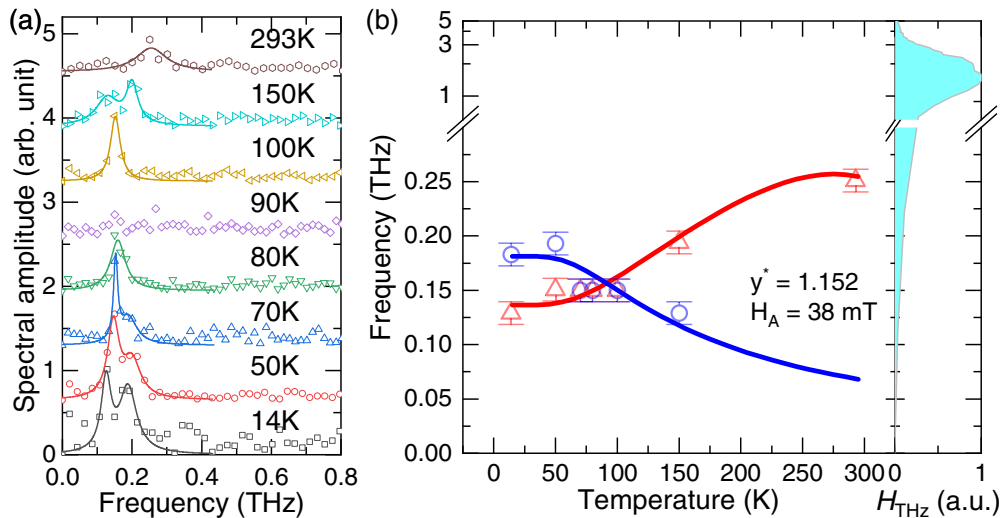


FIG. 4. (a) Fourier spectra of THz-induced polarization rotation at different temperatures. The solid lines correspond to the fit with two Lorentzian functions. The corresponding waveforms are shown in Appendix C. The THz electric-field strength is 500 kV/cm. (b) Frequency dependence of the q-AFM (red triangles) and the q-FM (blue circles) modes on temperature. The fits based on Eq. (4) are shown as solid curves. The spectrum of the THz pump pulse is shown from the right. To exclude contributions from the forced THz response, we start the Fourier time window at the end of the initial THz pulse (~ 3 ps).

coordinates, we write $\mathbf{L} = L(\sin \theta \cos \varphi, \sin \theta \sin \varphi, \cos \theta)$ and $\mathbf{M} = M_S(\sin \theta \cos \varphi, \sin \theta \sin \varphi, \cos \theta)$.

From the rectangular-shape hysteresis loops [Fig. 1(a)] we concluded that the magnetization is directed along the external magnetic-field \mathbf{H}_{ext} . Assuming \mathbf{H}_{ext} being sufficient to align magnetization, the ground state can be defined by two angles $\theta_0 = \pi/2$ and $\varphi_0 = \pi/2$. By writing and linearizing the Euler-Lagrange equations near θ_0 and φ_0 , the perturbation angles $\theta_1 = \theta - \theta_0$ and $\varphi_1 = \varphi - \varphi_0$ can be determined from the damped oscillator equations,

$$\begin{aligned} \ddot{\theta}_1 + \frac{2}{\tau} \dot{\theta}_1 + \omega_1^2 \theta_1 - (\omega_{\text{ex}} - \omega_H) \dot{\varphi}_1 + \omega_3^2 \varphi_1 &= \gamma \dot{H}_{\text{THz},x}, \\ \ddot{\varphi}_1 + \frac{2}{\tau} \dot{\varphi}_1 + \omega_2^2 \varphi_1 + (\omega_{\text{ex}} - \omega_H) \dot{\theta}_1 + \omega_3^2 \theta_1 &= \gamma \dot{H}_{\text{THz},z'} \approx \gamma \delta \dot{H}_{\text{THz},y}, \end{aligned} \quad (1)$$

where τ is a decay time, δ is the refraction angle for the THz light at the crystal surface, $\omega_{\text{ex}} = \gamma \lambda M_S$, $\omega_H = \gamma H_{\text{ext}}$, $\omega_1^2 = \gamma^2 \lambda (\frac{\partial^2 W}{\partial \theta^2})_{\theta=\theta_0, \varphi=\varphi_0}$, $\omega_2^2 = \gamma^2 \lambda (\frac{\partial^2 W}{\partial \varphi^2})_{\theta=\theta_0, \varphi=\varphi_0}$, and $\omega_3^2 = \gamma^2 \lambda (\frac{\partial^2 W}{\partial \varphi \partial \theta})_{\theta=\theta_0, \varphi=\varphi_0}$. $W(\theta, \varphi)$ is the magnetic anisotropy energy, and λ is the exchange parameter. Neglecting damping ($1/\tau = 0$) and external magnetic-field contribution ($\omega_H \ll \omega_{\text{ex}}$), the characteristic equation can be written in the form

$$(\omega_1^2 - \omega^2)(\omega_2^2 - \omega^2) = \omega_{\text{ex}}^2 \omega^2 + \omega_3^4. \quad (2)$$

Then we derive frequencies of the q-AFM and q-FM modes,

$$\omega_{\text{q-AFM, q-FM}}^2 = \frac{1}{2} (\omega_1^2 + \omega_2^2 + \omega_{\text{ex}}^2) \left(1 \pm \sqrt{1 - 4 \frac{\omega_1^2 \omega_2^2 - \omega_3^4}{(\omega_1^2 + \omega_2^2 + \omega_{\text{ex}}^2)^2}} \right), \quad (3)$$

where \pm corresponds to two modes.

The anisotropy of the Bi,Ga-YIG film produced by liquid phase epitaxy consists of cubic, uniaxial, and biaxial anisotropies [23]. Usually the cubic anisotropy is small, whereas the rest strongly depends on composition and growth conditions [24]. Here $W = K_{\text{out}} \frac{M_x^2}{M_S^2} + K_{\text{in}} \frac{M_y^2}{M_S^2} + K_{\text{ort}} \frac{M_x M_y}{M_S^2}$, where K_{out} , K_{in} , and K_{ort} denote out-of-plane, in-plane, and canted orthorhombic anisotropy constants, correspondingly. To simplify fitting of experimentally obtained frequencies to Eq. (3), we neglect contribution from orthorhombic anisotropy ($\omega_3 = 0$) and assume equal in-plane and out-of-plane anisotropies $\omega_1^2 = \omega_2^2 = \gamma^2 \lambda L H_A$ with H_A being the anisotropy field. Then the solution of Eq. (3) can be written in the form of the Kittel-Kaplan formula,

$$\frac{\omega_{\text{q-AFM, q-FM}}}{2\pi} = \frac{\gamma}{2} [\lambda^2 M_S^2 + 4\lambda H_A L]^{1/2} \pm \frac{\gamma}{2} \lambda M_S, \quad (4)$$

where we use $\lambda \approx -45$ Tesla/ μ_B [14]. To estimate the magnitude of the anisotropy field, we use the data from Ref. [25]. The sublattice magnetizations were estimated from molecular-field theory (see Appendix A). The fit [solid curves in Fig. 4(b)] according to Eq. (4) shows very good agreement with experimental data. In the vicinity of compensation point exchange term $\sim \lambda^2 M_S^2$ is comparable with anisotropy term $\sim \lambda L H_A$ leading to the q-FM and q-AFM frequencies being close to each other.

Temperature dependences of the q-FM and q-AFM modes allow to conclude that the excitation is resonant. In Fig. 4(b) the spectrum of the THz pump pulse is plotted against the magnetic mode frequencies. One sees that both modes are observed only when there is a spectral density in the excitation pulse at the frequency of the modes. As the temperature increases, the q-FM mode disappears in the detected signal as its frequency softens beyond the spectral range of the THz pulse. It is worth noting that quadratic on THz-field terms can also contribute to off-resonant excitation of magnetic modes,

e.g., via the THz inverse Cotton-Mouton effect [13], although relatively high-mode frequency with respect to the THz pulse spectrum width considerably diminishes its efficiency.

The THz magnetic-field $\mathbf{H}_{\text{THz}} \parallel \mathbf{x}_0$ hampers observation of the magnetic modes. At the moment of the THz pulse excitation, the out-of-plane $\theta_1 \sim \gamma \dot{H}_{\text{THz},x}$ and in-plane $\varphi_1 \sim \gamma \delta \dot{H}_{\text{THz},y}$ components of magnetization are mostly determined by the external torques. Noting that the Faraday rotation is mostly sensitive to the out-of-plane component of magnetization and, thus, to θ_1 , one readily sees that the forced response is well pronounced at $\mathbf{H}_{\text{THz}} \parallel \mathbf{x}_0$. As a result, this forced contribution following a THz pulse shape masks oscillations at magnetic mode frequency, which are also driven by $\gamma \dot{H}_{\text{THz},x}$. On the other hand, the THz magnetic-field $\mathbf{H}_{\text{THz}} \parallel \mathbf{y}_0$ refracts at the inclined crystal surface and results in nonzero z' projection of the THz magnetic-field $H_{\text{THz},z'} = H_{\text{THz},y} \sin \delta \approx \delta H_{\text{THz},y}$. The torque $\gamma \delta \dot{H}_{\text{THz},y}$ triggers dynamics of the in-plane component of magnetization described by φ_1 , which, in turn, result in the out-of-plane θ_1 component movement detected in the experiment.

Interestingly, from comparing the temporal signals excited by $\mathbf{H}_{\text{THz}} \parallel \mathbf{x}_0$ and $\mathbf{H}_{\text{THz}} \parallel \mathbf{y}_0$ [Fig. 2(a)] one sees that the amplitudes of the oscillation of θ_1 at the frequency of the magnetic mode [see the spectral weight along the dotted line in Fig. 2(b)] are comparable when driven by $\gamma \dot{H}_{\text{THz},x}$ and by $\gamma \delta \dot{H}_{\text{THz},y}$, despite $\delta \ll 1$. Efficient excitation of oscillations of θ_1 observed in the latter case can be explained by the ellipticity of the excited modes. Ellipticity is defined by intrinsic properties of the spin system and can be introduced

as a ratio of $\frac{\theta_1}{\varphi_1} \sim \frac{\omega_2^2 + i\omega_{\text{ex}}\omega_{\text{q-FM, q-AFM}}}{\omega_1^2 - \omega_{\text{q-FM, q-AFM}}^2} = \sqrt{\frac{\omega_2^2 - \omega_{\text{q-FM, q-AFM}}^2}{\omega_1^2 - \omega_{\text{q-FM, q-AFM}}^2}} \exp(i\zeta)$,

where $\tan \zeta = \frac{\omega_{\text{ex}}\omega_{\text{q-FM, q-AFM}}}{\omega_3^2}$. Except in the vicinity of the compensation point, all frequencies here are of the same order of magnitude [17] and we can assume $\theta_1/\varphi_1 \approx \pm 1$. This allows us to conclude that excitation of the dynamics of the out-of-plane magnetization component θ_1 mediated by the

coupling of the THz field to the in-plane component φ_1 is as efficient as the direct coupling of the THz field to θ_1 . Earlier, such a scenario for efficient excitation relying on pronounced ellipticity of magnetic modes has been realized for the case of optical excitation of magnetic dynamics in a weak ferromagnet [26]. Moreover, the imaginarity of θ_1/φ_1 induces coupling of a linear-polarized THz pump to both q-AFM and q-FM modes simultaneously as indeed observed in our experiments at $T < 150$ K (Fig. 4). It is worth noting that a giant linear magnetoelectric effect [27] was reported in a (210)-cut yttrium iron garnet thin film, which can add additional components to the torque. At the same time, the magnetoelectric tensor usually depends on temperature [28], whereas a pronounced temperature dependence of the spin modes amplitudes has not been observed experimentally.

Resonant excitation of the magnetic modes by the THz magnetic field in a ferrimagnet can be enhanced if the sublattices possess different gyromagnetic ratios [8]. Unambiguously, in the studied sample, the gyromagnetic ratios of iron ions in tetrahedral and octahedral sites are the same $\gamma_O = \gamma_T = \gamma$. Nevertheless, magneto-optical susceptibilities of the two sublattices are still different and may affect the optical detection of the excited modes. To examine why the observed magnetization dynamics is well observable, we first estimated normalized THz-induced rotation associated with the excited magnetic mode as $d\theta_F/\theta_F \sim 1 \text{ mdeg}/10^\circ = 10^{-4}$, where $d\theta_F$ is the amplitude of the probe polarization rotation induced by the THz pump (see Appendix C), and θ_F is the static Faraday rotation in remanence [see Fig. 1(a)]. Next, we analytically solved the system of coupled Landau-Lifshitz equations for two ferrimagnetic sublattices [22],

$$\frac{d\mathbf{M}_i}{dt} = -\gamma\mathbf{M}_i \times \mathbf{H}_i^{\text{eff}} + \frac{\alpha_i^G}{M_i}\mathbf{M}_i \times \frac{d\mathbf{M}_i}{dt}, \quad (5)$$

where the magnetization of the sublattices $M_i = M_T$ and M_O , Gilbert damping factors are $\alpha_i^G = \alpha_O^G$ and α_T^G , and the effective fields are $\mathbf{H}_i^{\text{eff}} = \mathbf{H}_{T,O}^{\text{eff}} = \mathbf{H}_{\text{THz}} + \mathbf{H}_{\text{ext}} - \lambda\mathbf{M}_{O,T} - \frac{\partial W}{\partial \mathbf{M}_{T,O}}$ [29]. To minimize influence of anisotropy, estimation is performed at room temperature. Then the probe polarization rotation is found noting that the Faraday rotation is the sum of the octahedral and tetrahedral contributions with different magneto-optical coefficients A and B , respectively,

$$\theta_F = AM_O + BM_T. \quad (6)$$

The gallium substitution leads to diamagnetic dilution and reduction of magneto-optical coefficients, whereas bismuth substitution enhances them by creating a strong dominance of the tetrahedral sublattice contribution [16,20]. According to the literature, a reasonable ratio for the studied garnet film is $B \approx -2A$. Figure 5(a) shows the simulated relative THz-induced Faraday rotation $d\theta_F/\theta_F$ at $\mathbf{H}_{\text{THz}} \parallel \mathbf{y}_0$ obtained using this ratio between A and B coefficients. One sees that the result of the numerical simulations appears to be of the same order of magnitude as in experiment $d\theta_F/\theta_F \sim 10^{-4}$. It is important to note that the difference in magneto-optical coefficients for two sublattices enhances $d\theta_F/\theta_F$ as demonstrated in Fig. 5(b). For instance, $B \approx -2A$ enhances the amplitude of the detected signal by a factor of 5 as compared to the case with equal coefficients $B \approx -A$. This also explains why magnetization

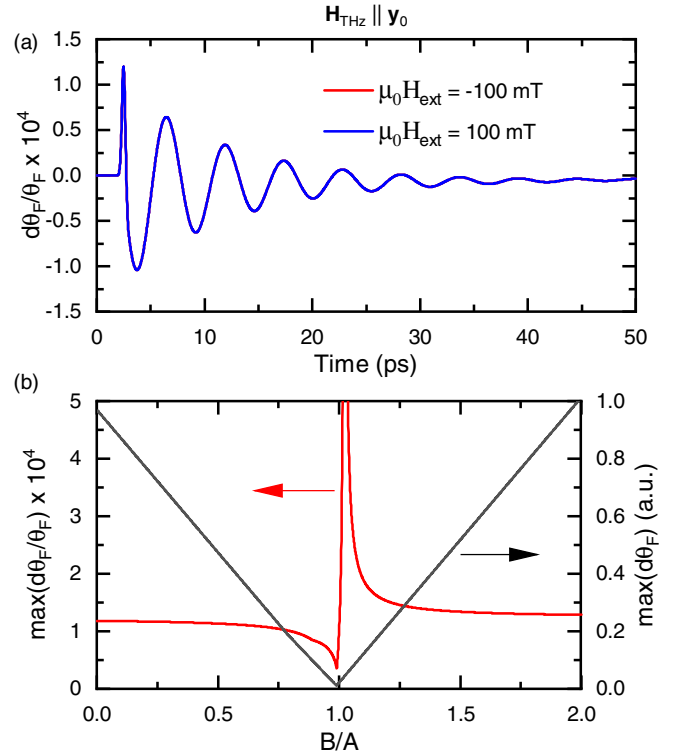


FIG. 5. (a) Numerical simulation of the relative THz-induced Faraday rotation at room temperature. The following parameters were used: the THz magnetic field of 160 mT, the exchange constant $\lambda \approx -45$ Tesla/ μ_B , the gyromagnetic ratio $\gamma = 28$ GHz/T, the ratio of magneto-optical coefficients $B/A = 2$, the saturation magnetization $M_S = 0.15 \mu_B$ and the external magnetic-field $H_{\text{ext}} = 100$ mT oriented at an angle 9° from the y axis. The Gilbert damping coefficients were taken in accordance with the experimental observation $\alpha_T^G = \alpha_O^G = 0.005$. The q-AFM mode is clearly visible. The mode is even with respect to the sign of the external magnetic field. (b) Maximum and relative THz-induced Faraday rotations as functions of the ratio of the magneto-optical coefficients B/A .

dynamics is observable even near the compensation point, where $M_S \approx 0$, whereas $\theta_F \approx (A + B)M_{O,T}$.

V. CONCLUSION

We experimentally show that intense THz pulses can simultaneously excite the q-AFM and the q-FM modes in a thin film of $(Y_{3-z}Bi_z)[Fe_{2-x}Ga_x][Fe_{3-y}Ga_y]O_{12}$ yttrium iron garnet in the vicinity of compensation point. The temperature dependence of the modes frequencies obtained from the theoretical formalism is in full agreement with the experimental data. The THz magnetic-field direction strongly affects the observation of the magnetic modes. Simultaneous excitation of both magnetic modes with the help of a linear-polarized THz pump is explained to be due to a strong ellipticity of the modes. Numerical simulations based on the Landau-Lifshitz-Gilbert equations show that an enhanced sensitivity of the magneto-optical effects to the magnetization dynamics is achieved due to a difference in magneto-optical susceptibilities of the two antiferromagnetically coupled iron sublattices.

ACKNOWLEDGMENTS

We thank P. Albers, Dr. S. Semin, and C. Berkhout for technical support, and M. V. Zamoryanskaya for the cathodoluminescence measurements. The research was funded by The Netherlands Organization for Scientific Research (NWO) and the Deutsche Forschungsgemeinschaft (DFG, German Research Foundation) - Project No. 277146847 - CRC 1238. The contribution of A.G.Z. has been funded by the Ministry of Science and Higher Education of the Russian Federation (Grant No. FSWR-2021-011). The contribution of A.K.Z. was supported by the Ministry of Science and Higher Education of the Russian Federation (Project No. 075-15-2022-1131). The contribution of A.M.K. was supported by the Russian Science Foundation (Grant No. 20-42-04405).

APPENDIX A

According to the molecular-field theory for single crystals [14], one can estimate site compositions ($x \approx 0.1$ and $y \approx 1.2$) from the total Ga substitution $x + y = 1.3$ [see Fig. 6(a)]. Corresponding saturation magnetization $M_S = M_O - M_T$ as a function of temperature is plotted in Fig. 6(b). It is seen that for $y \approx 1.2$ saturation magnetization M_S does not fit experimental observation (the blue dashed curve). The difference can be related to the growth conditions, which can affect

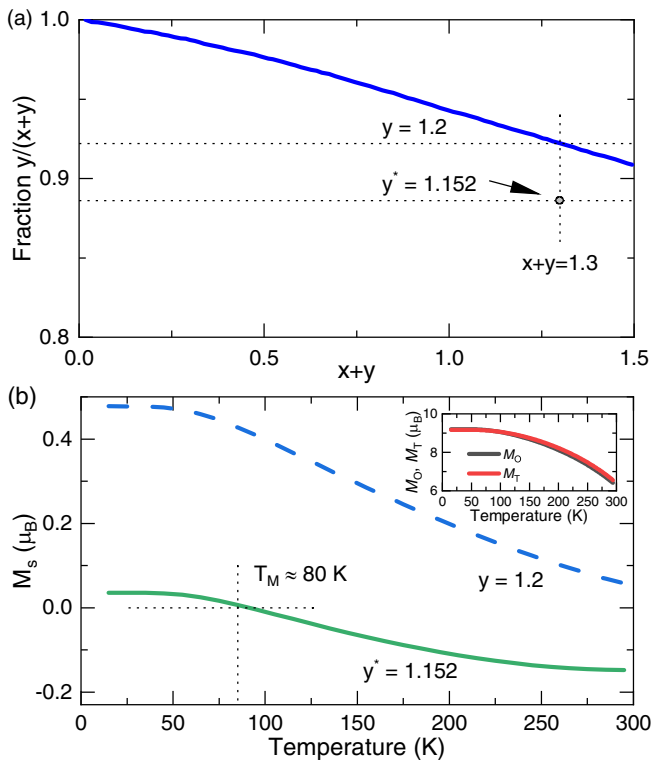


FIG. 6. (a) Fraction $y/(x+y)$ vs total gallium substitution $x+y$ (blue curve) adopted from Ref. [14]. The point $y^* = 1.152$ corresponds to the fraction value estimated from the experimentally observed compensation temperature. (b) Saturation magnetization $M_S = M_O - M_T$ as a function of temperature for $y = 1.2$ (blue dashed curve) and $y^* = 1.152$ (green curve). $M_O(T)$ and $M_T(T)$ temperature dependencies are shown in the inset.

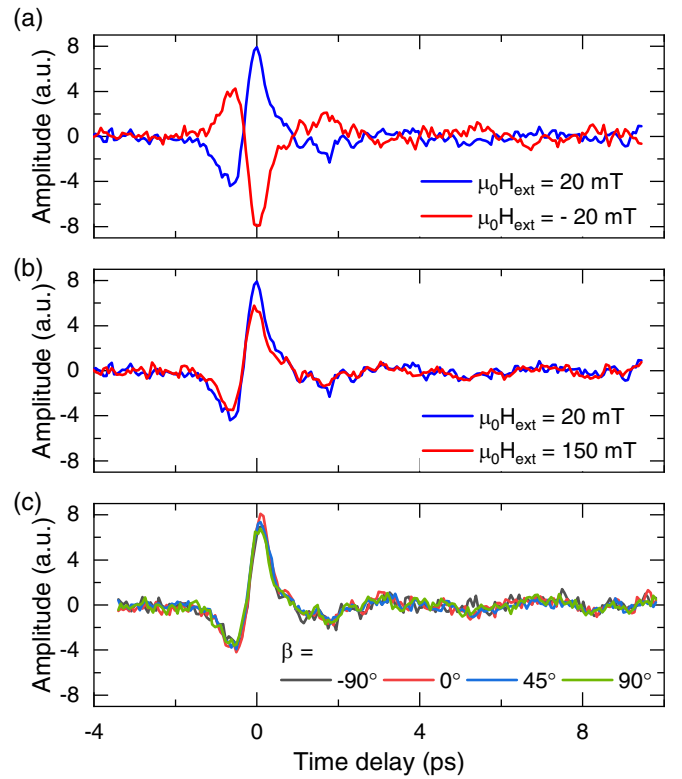


FIG. 7. The THz-induced probe polarization rotation at (a) opposite polarities and (b) different strengths of the external magnetic-field \mathbf{H}_{ext} . (c) Dependence on probe polarization angle β . $\mathbf{H}_{\text{THz}} \parallel \mathbf{x}_0$ and $T = 292$ K. The dominant contribution from the forced response $\sim \gamma \dot{H}_{\text{THz},x}$ is observed.

the distribution of gallium on tetrahedral and octahedral sites [30]. Hence, alternatively, the sites compositions x and y can be estimated from the observed compensation temperature $T_M \approx 80$ K. The best agreement with experiments is given by $x^* \approx 0.148$ and $y^* \approx 1.152$ (the green curve). Note that the bismuth substitution mainly affects the high-temperature magnetization through its effect on the superexchange interaction [31].

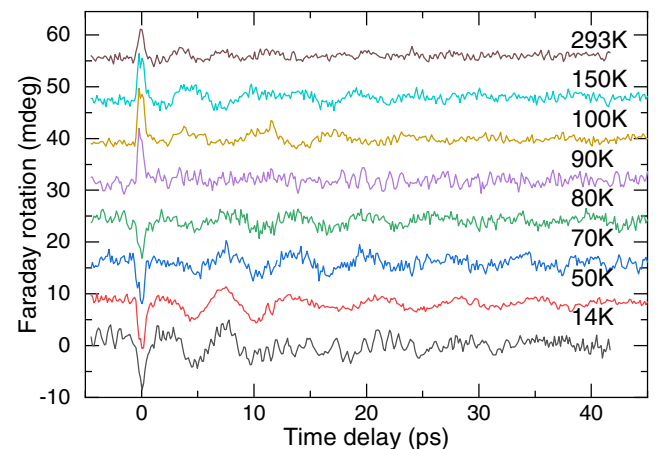


FIG. 8. The THz-induced probe polarization rotation measured at different temperatures indicated near corresponding curves.

APPENDIX B

Figure 7 depicts how the THz-induced dynamics with $\mathbf{H}_{\text{THz}} \parallel \mathbf{x}_0$ depends on the external magnetic field \mathbf{H}_{ext} and the probe polarization angle β .

APPENDIX C

Figure 8 depicts the waveforms of the THz-induced polarization rotation used for plotting Fourier spectra in Fig. 4(a).

- [1] F. Arute, K. Arya, R. Babbush, D. Bacon, J. C. Bardin, R. Barends, R. Biswas, S. Boixo, F. G. S. L. Brandao, D. A. Buell *et al.*, Quantum supremacy using a programmable superconducting processor, *Nature (London)* **574**, 505 (2019).
- [2] P. Némec, M. Fiebig, T. Kampfrath, and A. V. Kimel, Antiferromagnetic opto-spintronics, *Nat. Phys.* **14**, 229 (2018).
- [3] C. D. Stanciu, F. Hansteen, A. V. Kimel, A. Kirilyuk, A. Tsukamoto, A. Itoh, and T. Rasing, All-Optical Magnetic Recording with Circularly Polarized Light, *Phys. Rev. Lett.* **99**, 047601 (2007).
- [4] S. M. Rezende, A. Azevedo, and R.L. Rodríguez-Suárez, Introduction to antiferromagnetic magnons, *J. Appl. Phys.* **126**, 151101 (2019).
- [5] H. Hirori, A. Doi, F. Blanchard, and K. Tanaka, Single-cycle terahertz pulses with amplitudes exceeding 1 MV/cm generated by optical rectification in LiNbO₃, *Appl. Phys. Lett.* **98**, 091106 (2011).
- [6] A. K. Zvezdin, Field induced phase transitions in ferrimagnets, *Handbook of Magnetic Materials* (Elsevier, Amsterdam, 1995), Vol. 9, Chap. 4, pp. 405–543.
- [7] M. Deb, P. Molho, B. Barbara, and J.-Y. Bigot, Controlling laser-induced magnetization reversal dynamics in a rare-earth iron garnet across the magnetization compensation point, *Phys. Rev. B* **97**, 134419 (2018).
- [8] T. G. H. Blank, K. A. Grishunin, E. A. Mashkovich, M. V. Logunov, A. K. Zvezdin, and A. V. Kimel, THz-Scale Field-Induced Spin Dynamics in Ferrimagnetic Iron Garnets, *Phys. Rev. Lett.* **127**, 037203 (2021).
- [9] S. Baierl, M. Hohenleutner, T. Kampfrath, A. K. Zvezdin, A. V. Kimel, R. Huber, and R. V. Mikhaylovskiy, Nonlinear spin control by terahertz-driven anisotropy fields, *Nat. Photonics* **10**, 715 (2016).
- [10] T. Kampfrath, A. Sell, G. Klatt, A. Pashkin, S. Mährlein, T. Dekorsy, M. Wolf, M. Fiebig, A. Leitenstorfer, and R. Huber, Coherent terahertz control of antiferromagnetic spin waves, *Nat. Photonics* **5**, 31 (2011).
- [11] T. Satoh, S.-J. Cho, R. Iida, T. Shimura, K. Kuroda, H. Ueda, Y. Ueda, B. A. Ivanov, F. Nori, and M. Fiebig, Spin Oscillations in Antiferromagnetic NiO Triggered by Circularly Polarized Light, *Phys. Rev. Lett.* **105**, 077402 (2010).
- [12] K. Grishunin, E. A. Mashkovich, A. V. Kimel, A. M. Balbashov, and A. K. Zvezdin, Excitation and detection of terahertz coherent spin waves in antiferromagnetic α -Fe₂O₃, *Phys. Rev. B* **104**, 024419 (2021).
- [13] E. A. Mashkovich, K. A. Grishunin, R. V. Mikhaylovskiy, A. K. Zvezdin, R. V. Pisarev, M. B. Strugatsky, P. C. M. Christianen, T. Rasing, and A. V. Kimel, Terahertz Optomagnetism: Nonlinear THz Excitation of GHz Spin Waves in Antiferromagnetic FeBO₃, *Phys. Rev. Lett.* **123**, 157202 (2019).
- [14] P. Hansen, P. Röschmann, and W. Tolksdorf, Saturation magnetization of gallium-substituted yttrium iron garnet, *J. Appl. Phys.* **45**, 2728 (1974).
- [15] E. Jesenska, T. Yoshida, K. Shinozaki, T. Ishibashi, L. Beran, M. Zahradnik, R. Antos, M. Kučera, and M. Veis, Optical and magneto-optical properties of Bi substituted yttrium iron garnets prepared by metal organic decomposition, *Opt. Mater. Express* **6**, 1986 (2016).
- [16] P. Hansen and J.-P. Krumme, Magnetic and magneto-optical properties of garnet films, *Thin Solid Films* **114**, 69 (1984).
- [17] L. A. Shelukhin, V. V. Pavlov, P. A. Usachev, P. Y. Shamray, R. V. Pisarev, and A. M. Kalashnikova, Ultrafast laser-induced changes of the magnetic anisotropy in a low-symmetry iron garnet film, *Phys. Rev. B* **97**, 014422 (2018).
- [18] J. Hebling, G. Almási, I. Kozma, and J. Kuhl, Velocity matching by pulse front tilting for large area THz-pulse generation, *Opt. Express* **10**, 1161 (2002).
- [19] D. H. Auston and M. C. Nuss, Electrooptical generation and detection of femtosecond electrical transients, *IEEE J. Quantum Electron.* **24**, 184 (1988).
- [20] P. Hansen and K. Witter, Magneto-optical properties of gallium-substituted yttrium iron garnets, *Phys. Rev. B* **27**, 1498 (1983).
- [21] G. A. Smolenskii, R. V. Pisarev, and I. G. Siniĭ, Birefringence of light in magnetically ordered crystals, *Sov. Phys. Usp.* **18**, 410 (1975).
- [22] M. D. Davydova, K. A. Zvezdin, A. V. Kimel, and A. K. Zvezdin, Ultrafast spin dynamics in ferrimagnets with compensation point, *J. Phys.: Condens. Matter* **32**, 01LT01 (2020).
- [23] P. Hansen and K. Witter, Growth-induced uniaxial anisotropy of bismuth-substituted iron-garnet films, *J. Appl. Phys.* **58**, 454 (1985).
- [24] I. Nistor, C. Holthaus, S. Tkachuk, I. D. Mayergoyz, and C. Krafft, Magnetic anisotropies in (210)-oriented bismuth substituted iron garnet thin films, *J. Appl. Phys.* **101**, 09C526 (2007).
- [25] P. Hansen, Anisotropy and magnetostriction of gallium-substituted yttrium iron garnet, *J. Appl. Phys.* **45**, 3638 (1974).
- [26] A. M. Kalashnikova, A. V. Kimel, R. V. Pisarev, V. N. Gridnev, P. A. Usachev, A. Kirilyuk, and T. Rasing, Impulsive excitation of coherent magnons and phonons by subpicosecond laser pulses in the weak ferromagnet FeBO₃, *Phys. Rev. B* **78**, 104301 (2008).
- [27] B. B. Krichevstov, V. V. Pavlov, and R. V. Pisarev, Giant linear magnetoelectric effect in garnet ferrite films, *JETP Lett.* **49**, 466 (1989).
- [28] M. Mostovoy, A. Scaramucci, N. A. Spaldin, and K. T. Delaney, Temperature-Dependent Magnetoelectric Effect from First Principles, *Phys. Rev. Lett.* **105**, 087202 (2010).
- [29] A. Kirilyuk, A. V. Kimel, and T. Rasing, Ultrafast optical manipulation of magnetic order, *Rev. Mod. Phys.* **82**, 2731 (2010).
- [30] P. Hansen, K. Witter, and W. Tolksdorf, Magnetic and magneto-optic properties of Bismuth- and aluminum-substituted iron garnet films, *J. Appl. Phys.* **55**, 1052 (1984).
- [31] S. Geller, H. J. Williams, G. P. Espinosa, R. C. Sherwood, and M. A. Gilleo, Reduction of the preparation temperature of polycrystalline garnets by bismuth substitution, *Appl. Phys. Lett.* **3**, 21 (1963).